Supplementary Material for
Distinct cell shapes determine accurate chemotaxis

Luke Tweedy, Börn Meier, Jürgen Stephan,
Doris Heinrich, Robert G. Endres

Contents

List of Figures
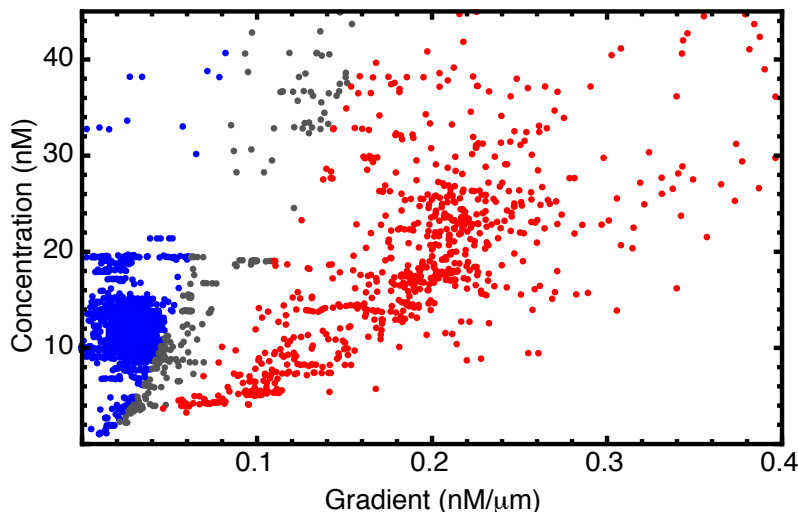
1 Supplementary figures

Figure S1: **Gradient-concentration pairs for low and high SNR.** Each dot is derived from the gradient and concentration at an instant in a trajectory taken from live-cell data. These gradients and concentrations were used to calculate SNRs. Blue and red points correspond to low and high SNR data, respectively. Points in grey are in neither category.
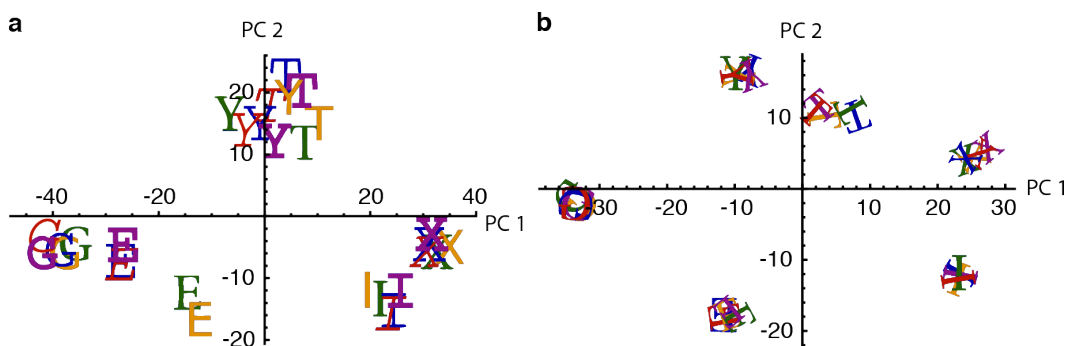
Figure S2: **Discrimination and rotational invariance of power spectra.** **a.** The projection of various letters in a number of different fonts into the first two components of their own shape space. The grouping of letters by shared features shows the discriminative power of PCA and power spectrum shape description, e.g. the relative closeness of T and Y due to sharing a stem with two prongs leaving the top. **b.** Random rotations of letters of the same font, projected into the same space, demonstrating the rotational invariance of shape analysis using power spectra.
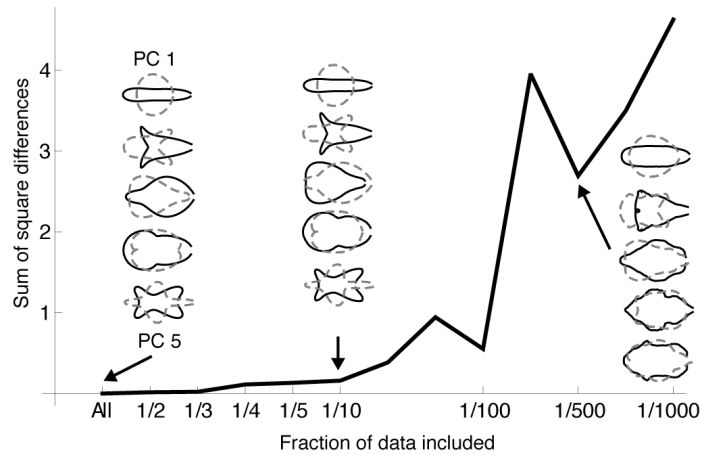
Figure S3: **Robustness of principal shape modes.** The sum of squared differences between the first 5 PCs as calculated using the whole data set and using smaller fractions of the data set. Examples of the first 5 PCs are shown for the whole, 1/10th and 1/500th of the data set.
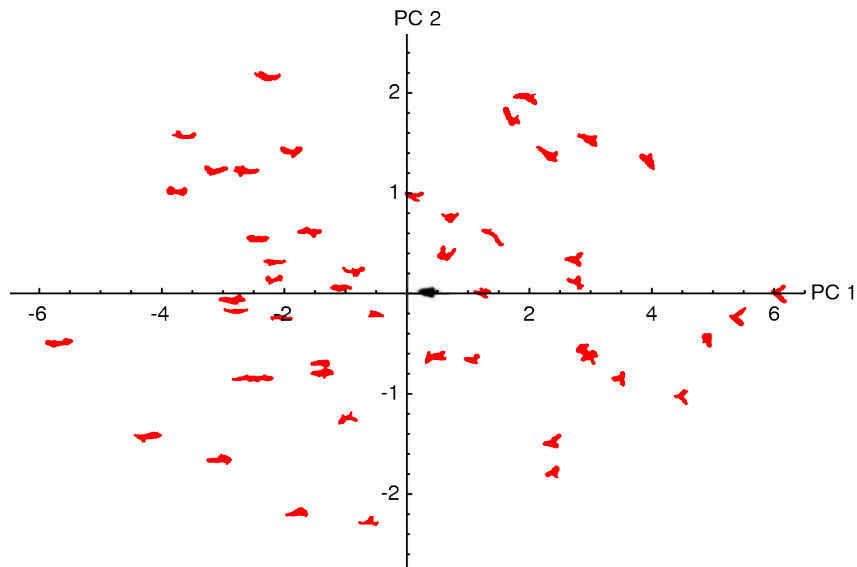
Figure S4: **Principal shape components from diffeomorphic mapping.** A set of cell shapes projected into the first two PCs as determined by large deformation diffeomorphic metric mapping. PC 1 is largely defined by pseudopod splitting. A residual dependence on orientation is apparent in PC 2. The black shape toward the center shows the Frechét mean of the set of shapes.
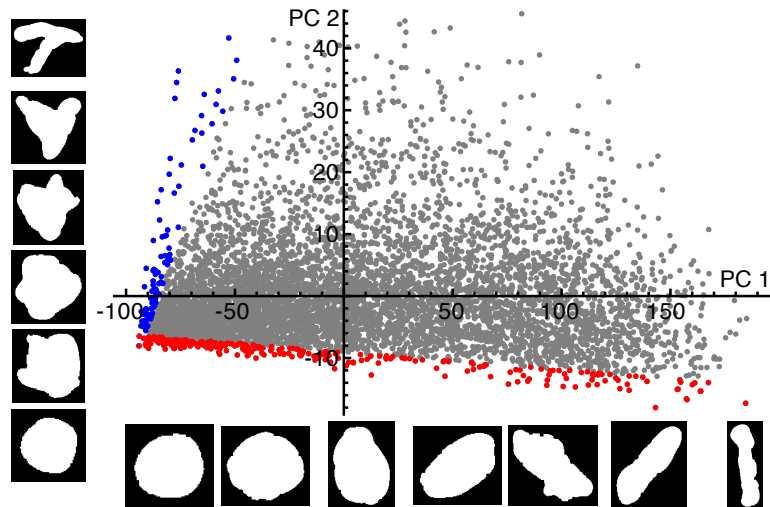
Figure S5: **Shape space exhibits sharp boundaries for PC 1 and PC 2.** A selection of coordinates for natural shapes in PCs 1 and 2 (grey dots). Shapes highlighted in blue indicate the lower limit on PC 1, at which the aspect ratio is approximately one. A selection of these shapes is shown to the left of the main plot. Shapes highlighted in red indicate a lower limit on PC 2, at which there is little or no bending. A selection of these shapes is shown below the main plot.
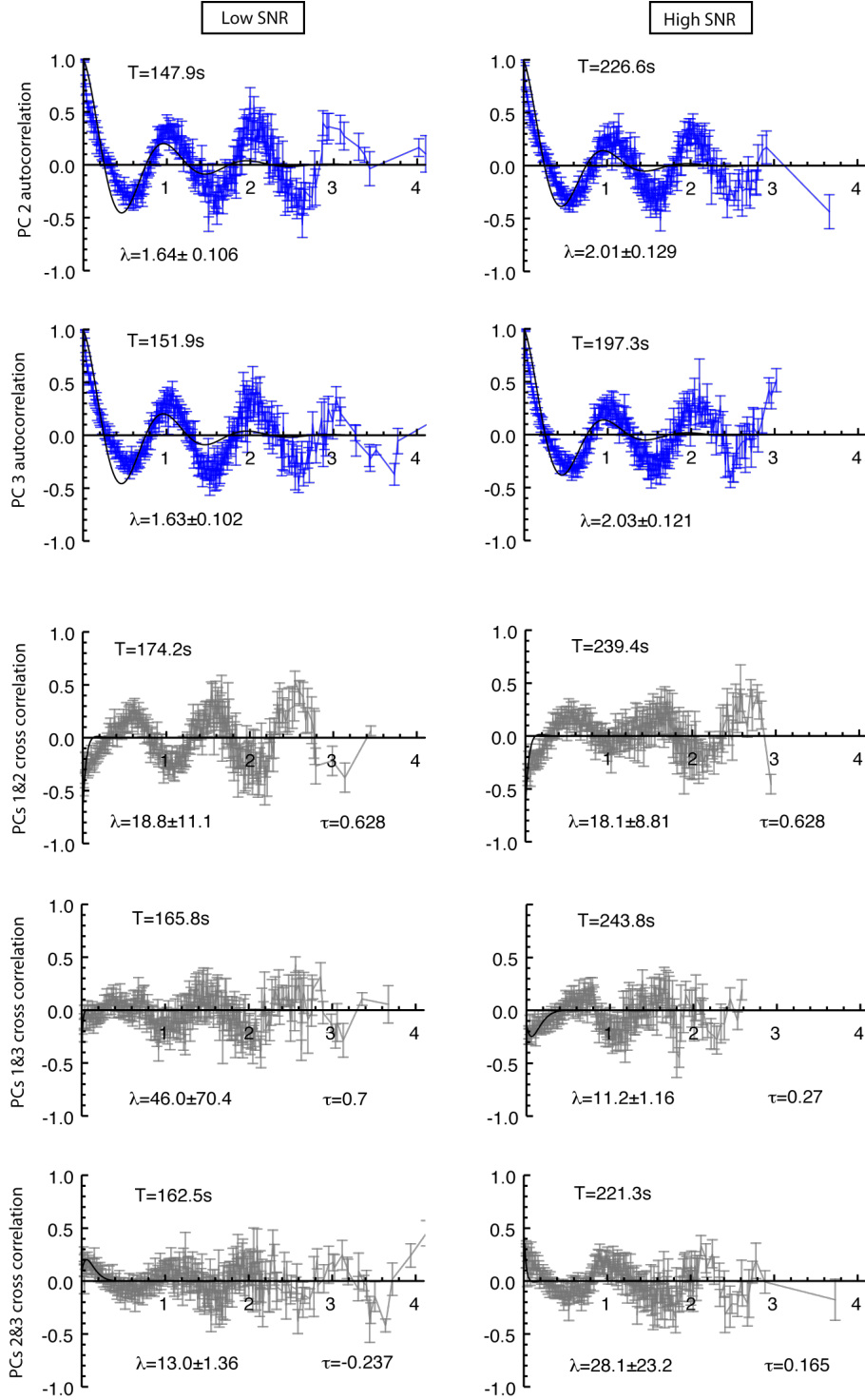
Figure S6: **Live cell auto- and cross-correlations in the first three PCs.** Additional auto- and cross-correlations. The median period in seconds T and fitted decay between peaks λ are shown in each case. As the cross-correlations need not start at 1, an additional offset parameter τ is shown as well. In this case λ and τ are taken by fitting $f(t) = e^{-\lambda+\tau}cos(2\pi t)$ to the mean value of the data. Note that T is consistently smaller for low SNR than for in the high SNR.

5
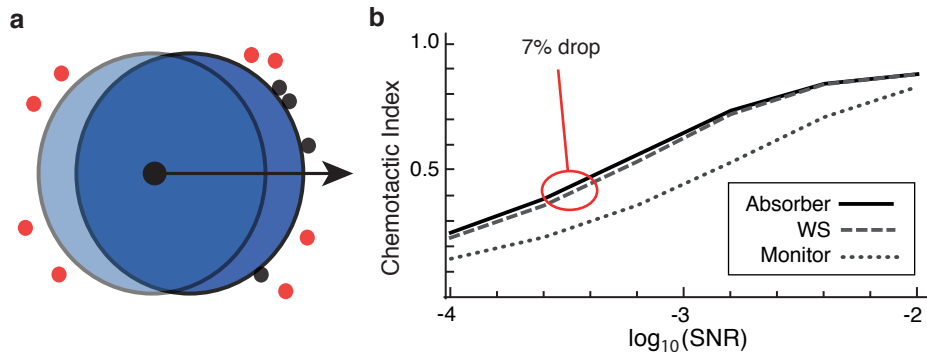
Figure S7: **The windshield effect due to cell movement.** **(a)** Diagram of the windshield effect. Unbound ligand (red) is more likely to be encountered by the cell in the direction of movement (black arrow), leading to preferential binding of ligand on its leading surface. **(b)** Predicted CIs in response to spatial chemical gradients for the perfect absorber with (WS, dashed line) and without (Absorber, solid line) windshield effect, and the perfect monitor (Monitor, dotted line), which does not remove ligand molecules from the environment after binding and so experiences noise from rebinding (16). The windshield effect causes a drop in the expected CI of around 7% in the low-SNR range (highlighted in red). The windshield effect is calculated for cells moving at $12\mu m/min$ in a 20nm cAMP background.
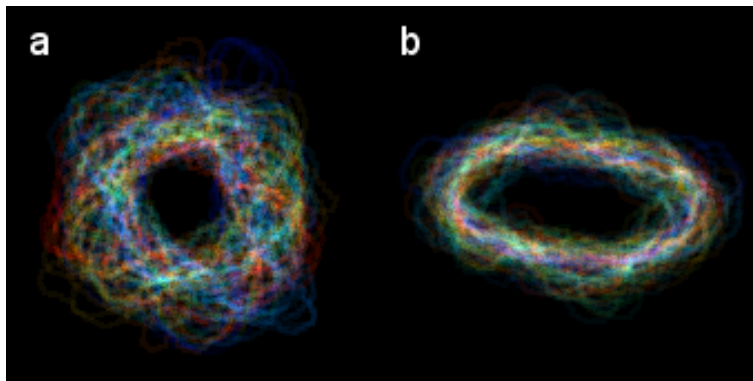
Figure S8: **Shape alignment methods.** The outlines of cells as aligned by direction of motion (a) and as aligned by Feret angle (b). In achieving a global alignment for all cells, any two cells are unlikely to be ideally aligned with each other.

6
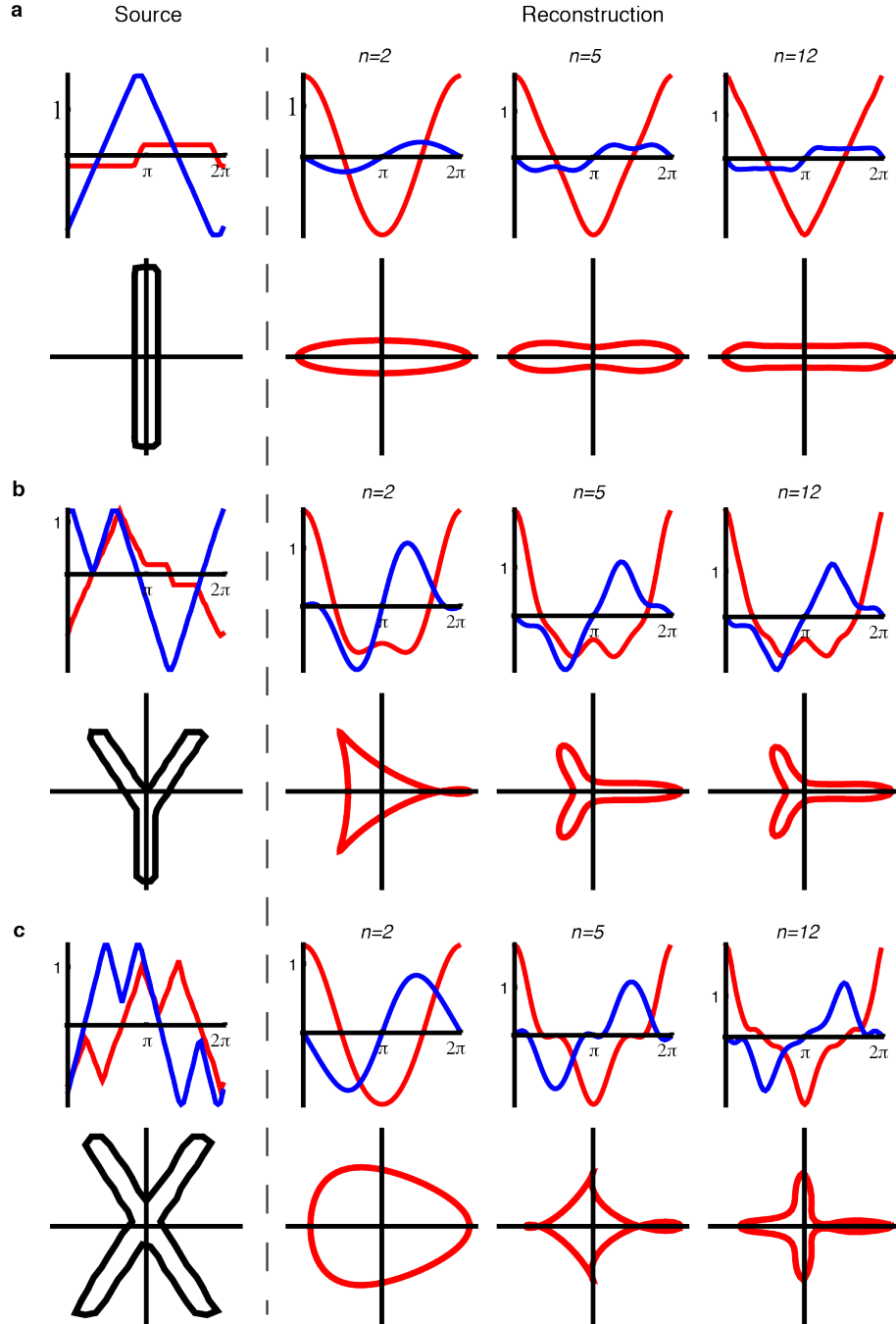
Figure S9: **Testing Fourier shape descriptors using letters from the alphabet.** **a-c.** Each source letter (bottom-left of each panel) can be decomposed into the real (red) and imaginary (blue) components of a complex function describing its outline. After power spectra are taken, the real and imaginary parts can be recovered and the shapes reconstructed. Reconstructions are shown using $n = 2, 5$ and 12 frequency terms. The letters I (a), Y (b) and X (c) are shown in reconstruction, verifying that power spectra can be used to recreate shape features up to orientation.
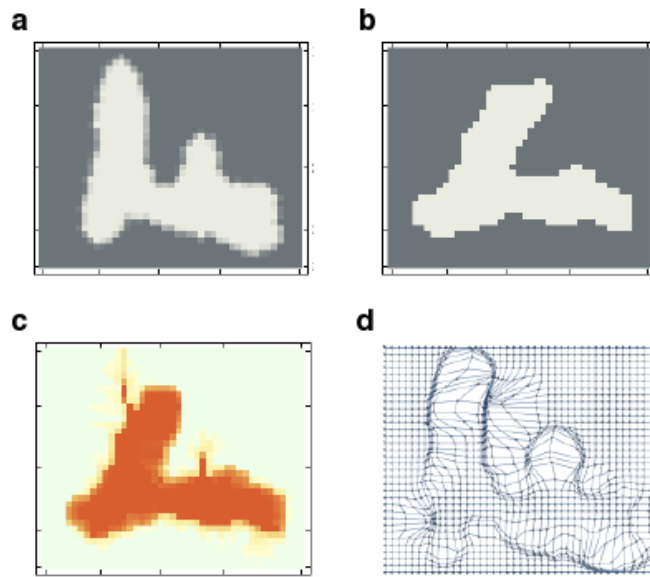
Figure S10: **An illustrative example of diffeomorphic mapping.** **a.** The source image, which is a binary mask of a migrating *D. discoideum* cell. **b.** The target image onto which the source is mapped. **c.** The resultant image after mapping from (a) to (b). **d.** The same mapping of (a) onto (b) represented by a shift of grid points.

2 Materials and methods

2.1 Cell culture

All wild-type cells are derived from the *Dictyostelium discoideum* AX2 strain. Cells are grown in AX2 nutrition medium, containing $10\mu g/mL$ Geneticin 418 disulfate salt (G418) (Sigma-Aldrich) and $10\mu g/mL$ Blasticidine S hydrochloride (Sigma-Aldrich). Cells are concentrated to $c = 5 \times 10^6$ cells$/mL$ in shaking culture (150 rpm). Five hours prior to the experiment, cells are washed with $17mM$ K-Na PBS pH 6.0 (Sigma-Aldrich). Four hours prior to the experiment, cells are pulsed with 200nM cAMP every 6 minutes. They are then introduced into the microfluidic chamber at $c = 2.5 \times 10^5$cells$/mL$. cAMP is added as a chemoattractant at concentrations between $c = 0nM$ and $c = 50nM$. Measurements are performed with cells starved for 5-7 h.

2.2 Microfluidics and imaging

The microfluidic device is made of a μ-slide 3-in-1 microfluidic chamber (Ibidi) as described in (19), with three $0.4 \times 1.0mm^2$ inflows that converge under an angle of $\alpha = 32°$ to the main channel of dimension $0.4 \times 3.0 \times 23.7mm^3$. Both side flows are connected to reservoirs, built from two $50ml$ syringes (Braun Melsungen AG), separately connected to a customised suction control pressure pump (Nanion). Two micrometer valves (Upchurch Scientific) reduce the flow velocities at the side flows. The central flow is connected to an infusion syringe pump (TSE Systems), which generates a stable flow of $1ml/h$. Measurements were performed with an Axiovert 135 TV microscope (Zeiss), with LD Plan-Neofluar objectives $20x/0.50N.A.$ and $40x/0.75N.A.$ (Zeiss) in combination with a DV2 DualView system (Photometrics). A solution of $1\mu M$ Alexa Fluor 568 hydrazide (Invitrogen) was used to characterise the concentration profile of cAMP (Sigma-Aldrich) because of their comparable molecular weight.

2.3 Image preprocessing

For every cell in each frame of a set of DIC videos, we extracted the centroid position and a binary mask using a custom-written plug-in for ImageJ. Cells were separated from the chamber background using Canny edge detection (34). The images were thresholded, with binary operations such as closing and filling applied to complete the cell mask. Data from frames in which cells touched was discarded in order to avoid polluting data with unwanted contact effects, such as distortions through contact pressure and cell-cell adhesion. The coordinates with respect to the centroid of 64 points around the perimeter of each binary image were encoded in a complex number such that each shape was a 64 dimensional vector of the form $\mathbf{S} = \mathbf{x} + i\mathbf{y}$. Each shape was transformed into the frequency domain using a fast Fourier transform. Principal component analysis was performed on the power spectra (with the power spectrum $P(f) = |s(f)|^2$ for the frequency-domain signal $s(f)$) to find the dominant modes of variation.

3 Supplementary discussion

3.1 The problem of shape

Shape is whatever geometric information there is in the surface of an object that is independent of its size, position and orientation. When using shape to describe features in multicellular organisms, it is easy to adhere to such a definition; specific anatomical features can be used to scale and align shapes accordingly, and shape variability is heavily restricted due to physiological concerns. Amoebae, on the other hand, have no fixed anatomical features. *D. discoideum* cell shape is particularly variable and any regularity of shape is largely a behavioural restriction. In order to satisfy the definition of shape, a method of shape quantification must overcome the problem of boundary alignment and give us a reliable measure of the similarity and dissimilarity of the shapes it encounters. A suitable method must also describe those features of a shape relevant to the problem under investigation.

3.2 Fourier shape descriptors

The method we choose employs Fourier shape descriptors, which have been applied to a number of biological problems with success (35–37). The boundary of each shape is treated as a complex function of distance along the contour, with the real part as the x coordinate and the imaginary part as the y coordinate. The function is trivially periodic, returning to any given point after traversing the length of its perimeter. This outline is sampled evenly, creating a discrete, complex-valued representation of the shape. The signal is moved into the frequency domain by means of a Fast Fourier transform, which accurately replicates the result of the discrete Fourier transform

$$X_k = \sum_{n=0}^{N-1} x_n e^{-2\pi ikn/N}. \tag{1}$$

The components X_k in the frequency domain each contribute to the description of the whole shape, where the spatial domain values x_n only describe local features. This is an advantage in our study, as we examine global shape changes involving the extension and retraction of large pseudopods and wish to emphasise such boundary-wide effects. Additionally, the magnitudes of the components X_k do not depend on the orientation of the data, as all orientation information is encoded in the phase and the initial point on the contour (see Fig. **S2** for an example using letters). This has numerous advantages over the standard approach to achieving orientation independence, namely image alignment. Most importantly methods that rely on aligning images still leave some dependence on rotation, often relying on best-fits for large data sets, which may be poor when comparing any two members (Fig. **S8**). Alignment methods leave sizable orientation dependence in our case, due to the staggering variability in cell shape in *D. discoideum*.

To quantify a cell's shape, we examine its power spectrum

$$P_k = X_k \cdot X_k^*, \tag{2}$$

10

which shares the rotational independence of the magnitudes of the X_k. Its primary use for us is due to its relationship to the autocorrelation of the boundary in the spatial domain. Given some discrete functions h_n, x_n and y_n with frequency domain counterparts H_k, X_k and Y_k, the convolution theorem states that

$$h_n = x_n \otimes y_n \Rightarrow H_k = X_k \cdot Y_k, \tag{3}$$

where $\otimes$ is the convolution operator. The power spectrum can thus be used to efficiently identify any repeated features of the boundary, such as pseudopodal projections, regardless of the shape's orientation (see Fig. **S9** for an illustrative example using letters).

In order to ensure that our PCs are robust to changes in the data used, we performed a shrinkage test, comparing the first six PCs for the whole dataset with the first 6 PCs generated using increasingly small subsets. In order to remove the effects of fluctuations in the contributions of PCs toward total variance, the magnitude all PCs were normalised. We found that differences only became substantial when calculating PCs using 2% (1/50th) of the data or less (see Fig. **S3**).

3.3   Alternative methods

There are a number of alternative methods that we initially explored, but found to be unsuitable for describing *D. discoideum* cell shape. In the following, we briefly describe these methods, the results we obtained by them and how this pertains to our analysis using Fourier shape descriptors.

3.3.1   Landmarks

The simplest method by which shape has been quantified takes the coordinates of significant features (or landmarks) on the surfaces of a set of shapes, and compares their respective positions (38). Shapes are more different from each other if their corresponding landmarks are further apart. Though easy to construct, these methods are only useful if two criteria are met: firstly, the data must be so morphologically similar that there is a clear correspondence of landmarks. Secondly, the landmarks must be obvious enough that their identification is a simple matter. The former (and so, trivially, the latter) is not the case for the shapes of *D. discoideum* cells.

A similar approach is to finely sample the boundary of a shape, taking the same number of points around the surface of each shape in a set, with the differences between shapes once more given by the distances between corresponding points (6). Though this method does not require that specific landmarks be identifiable (or even present), it nevertheless relies on the shape variability remaining low enough that corresponding points do not drift too far from each other, nor from any features they happen to describe. Due to these restrictions, this method is inadequate to capture the variability of *D. discoideum* cell shape.

3.3.2 Diffeomorphic mapping

A number of algorithms for shape analysis fall into the category of diffeomorphic mappings (39–41). These methods treat a shape as a continuum made from some physical substance with properties such as elasticity. This has a great appeal when working in cytometry, as a cell is itself such an object. Inherent in these methods is the exclusion of any physically meaningless result from the space of possible shapes: the mappings cannot tear an object, nor fold it over such that it is double valued in a single region.

For a position vector $\vec{x}$ and a displacement vector $d(\vec{x})$, the generic mapping $\phi(\vec{x})$ takes the form

$$\phi(\vec{x}) = \vec{x} + d(\vec{x}). \tag{4}$$

When mapping from a source shape I_0 to a target shape I_1, d is chosen to minimise the difference between the deformed source shape and the target

$$\tilde{d} = \arg\min_{d} \left\| I_0 \circ \phi - I_1 \right\|^2 \tag{5}$$

$$\arg\min_{d} f(d) := d | \forall s : f(d) \leq f(s), \tag{6}$$

where $\left\| f \right\|$ is the L^2 norm of any function f.

There are still an infinite number of mappings that satisfy Eq. (5). We limit our scope to the mappings that preserve the neighborhood. Informally these can be thought of as mappings that do not tear or fold shapes. This condition is enforced by the introduction of a differential operator, $\mathcal{L}$. In this case, $\tilde{d}$ takes the form

$$\tilde{d} = \arg\min_{d} \left\| \mathcal{L}d \right\|^2 + \frac{1}{\sigma^2} \left\| I_0 \circ \phi - I_1 \right\|^2. \tag{7}$$

An example of a diffeomorphic mapping of the kind described in Eq. (7) is shown in Fig. **S10**.

A number of choices exist for $\mathcal{L}$, including operators describing diffusion and fluid flow. A good choice is a linear elasticity operator, $\mathcal{L} = -\alpha\vec{\nabla}^2 + \gamma$, where α and γ are constants. Using such a choice, the difference between two shapes can be interpreted as the stress under which an elastic object would need to be placed in order to deform from the first shape to the second.

We applied a diffeomorphic method known as large deformation diffeomorphic metric mapping (40) (LDDMM) to the problem of *D. discoideum* cell shape. We first used ImageJ to produce binary masks covering the area occupied by the cell. We scaled each mask to unit area, then aligned them as follows: We produced a morphological skeleton of each mask, and centred each image according to the position of the most significant branch point in its skeleton. We then rotated each image to minimise the distance between the longest branches of the morphological skeleton.

LDDMM encapsulates the entirety of the mapping information in a vector of dimension $2N$, where N is the number of pixels in any one image. This vector gives the initial velocity with which each element in the source shape must move in order to evolve into the target

shape under the physical constraints imposed by $\mathcal{L}$. We calculated a velocity vector for every shape that mapped it to the Frechét mean of the data set. We then reduced the dimension of the system by performing principal component analysis (PCA) on these velocity vectors. The presence and size of pseudopods was found to be the main feature of the first principal component (PC 1), with the second component (PC 2) largely dependent on the angle of the principal axis of the shape (see Fig. **S4**).

The first two PCs derived using LDDMM are both heavily dependent on our method of image alignment. In the case of PC 1, our deliberate alignment by branching-points places heavy emphasis of pseudopods. This is not intrinsically problematic (indeed, we wish to find a method which emphasises the features we wish to understand). The problem with our method of alignment is more visible in PC 2. Alignment of the larger protrusions produces a great deal of variability in the relative angles of smaller protrusions. This variability is a key feature of PC 2, and it is largely an artifact of orientation. Nevertheless, we find it encouraging that our PC 1 as found using LDDMM shares features with PC 2 as found using Fourier shape descriptors.

In principle, the alignment dependence of LDDMM can be substantially reduced. Instead of trying to find a global best fit for all shapes as in Fig. **S8**, we can align each possible pairing of shapes in the set separately, and thus calculate the minimum distance between them, irrespective of orientation. A full compliment of these distances can be used to create a map of the shape space using multidimensional scaling. We chose to reject this approach because of the computational cost. As each shape must be compared with every other, the costs rise such that $T(n) \in O(n^2)$, making large datasets prohibitively costly.

3.4 Windshield effect

The perfect absorber model makes a prediction for the expected chemotactic index of cells as a function of the SNR they experience. In Fig. S7 we show how this prediction changes when the windshield effect is included. Here, we detail the derivation of the expected chemotactic indices for a perfect absorber, both with and without the windshield effect. The variance of the estimated chemical gradient for a perfect absorber is (16)

$$\langle (\delta c_x)^2 \rangle = \frac{c_0}{12 \pi D a^3 T}. \tag{8}$$

Assuming estimated gradients are Gaussian-distributed, and that there is an actual gradient c_0^y in the y direction, the two-dimensional distribution of estimated gradients $c_r = (c_x, c_y)$ is

$$P_{c_y^0}(c_x, c_y) = \frac{1}{2\pi\sigma^2} \left[e^{-c_x^2/2\sigma^2} e^{-(c_y - c_y^0)^2/2\sigma^2} \right]. \tag{9}$$

As the windshield effect contributes an apparent gradient $|\vec{\nabla} c| = v_0 c_0 / D$ (see main text), the distribution of estimated gradients for a moving absorber experiencing the windshield effect is:

$$P_{c_y^0}(c_x, c_y) = \frac{1}{2\pi\sigma^2} \left[e^{-\left(c_x - \frac{v_0 c_0}{D} \frac{c_x}{\sqrt{c_x^2 + c_y^2}}\right)^2/2\sigma^2} e^{-\left(c_y - \left(c_y^0 + \frac{v_0 c_0}{D} \frac{c_y}{\sqrt{c_x^2 + c_y^2}}\right)\right)^2/2\sigma^2} \right]. \tag{10}$$

13

In either case, the expected chemotactic index $\langle CI \rangle$ is given by

$$\langle CI \rangle = \iint_{-\infty}^{\infty} \frac{c_y}{\sqrt{c_x^2 + c_y^2}} P_{c_y^0}(c_x, c_y) dc_x dc_y, \tag{11}$$

which we integrate numerically.

3.5 Computational chemotaxis simulations

To better understand the importance of shape, as well as to connect our principal shape modes to biochemistry, we modelled cell shape and behaviour by evolving a contour $\Gamma(t)$ according to the concentrations of three simulated biochemical species. These species interact according to the Meinhardt model of biochemical pattern formation (21), recently implemented by (23), with chemosensing modified to represent the perfect absorber. At time t and a distance $\{\gamma \in \mathbb{R} | 0 < \gamma \leq |\Gamma(t)|\}$ around the contour, the three species are a local activator with concentration $a(\gamma, t)$, a global inhibitor with concentration $b(t)$ and a local inhibitor with concentration $c(\gamma, t)$. These three species evolve according to the following equations:

$$\frac{da(\gamma, t)}{dt} = D_a \frac{\partial^2 a(\gamma, t)}{\partial \gamma^2} + \frac{s(\gamma, t)\left(b_a + \frac{a(\gamma, t)^2}{b(t)}\right)}{(s_c + c(\gamma, t))(1 + s_a a(\gamma, t)^2)} - r_a a(\gamma, t), \tag{12}$$

$$\frac{db(t)}{dt} = \frac{r_b}{|\Gamma(t)|} \oint_{\Gamma(t)} a(\gamma, t) d\gamma - r_b b, \tag{13}$$

$$\frac{dc(\gamma, t)}{dt} = D_c \frac{\partial^2 c(\gamma, t)}{\partial \gamma^2} + b_c a(\gamma, t) - r_c c(\gamma, t). \tag{14}$$

In Eq. 12, D_a is the diffusion constant for a, b_a is the basal production rate of a, s_c is the Michaelis-Menten constant, and s_a determines the saturation point of a. In Eqn. 14, D_c is the diffusion constant for c, with $D_c > D_a$, and b_c is the production rate of b in the presence of a. Parameters r_a, r_b, r_c are the death rates of a, b and c respectively. The parameter $s(\gamma, t)$ is the chemosensation at membrane patch $(\gamma, \gamma + d\gamma)$ at a distance γ around the membrane and over a time dt:

$$s(\gamma, t) = r_a \left[A(1 + dr R) + J(\gamma, t)dt + X\sqrt{J(\gamma, t)dt} \right]. \tag{15}$$

The first term represents environment-independent stimulus (auto-activation), in which A is the magnitude of auto-activation, R is a random number in the interval $[-1, 1]$, and $dr < 1$ is a constant that determines the spread of the random contribution. The second term is absorber-like environmental stimulus, in which J is the flux of chemoattractant over the membrane patch $\gamma + d\gamma$ at time t. The third term is Poisson-like noise, with X a normally distributed random variable. In the second and third terms, J is given by:

$$J(\gamma, t) = 4Dc(\gamma, t)d\gamma, +J_{ws}(\gamma, t) \tag{16}$$

14

k_a	0.005	k_Γ	4.0×10^{-6}
k_θ	3.0	k_P	1.2×10^{-7}
r_b	0.05	b_c	0.0018
r_c	0.013	D_c	2.95
s_a	1.0×10^{-4}	b_a	0.1
r_a	0.02	D_a	1.5

Table 1: Constants in arbitrary units used in "wild type" simulations of chemotacting cells.

where $c(\gamma, t)$ is the concentration of chemoattractant at γ, t and D is the chemoattractant diffusion constant. $J_{ws}(\gamma, t)$ is the additional flux caused by the windshield effect on a line element $d\gamma$ with normal $\hat{\mathbf{n}}(\gamma)$ and velocity $\mathbf{v}$, and is given by:

$$J_{ws}(\gamma, t) = c(\gamma, t)\mathbf{v} \cdot \hat{\mathbf{n}}(\gamma)dA \tag{17}$$

for simulations that include the windshield effect. Here, $dA = d\gamma^2$.

The force acting on the boundary is determined by the combination of an outward force proportional to the local concentration of a, membrane tension and cytosolic pressure. For a natural membrane length of Γ_0, and a natural area of A_0, the force acting on the boundary is given by:

$$F(\gamma, t) = \left[k_a a(\gamma, t) - k_P\big(A(t) - A_0\big) - k_\Gamma\big(|\Gamma(t)| - \Gamma_0\big)\right]\hat{n}(\gamma, t), \tag{18}$$

where k_a, k_P and k_Γ are constants determining the influence of a, pressure and membrane tension respectively, and $\hat{n}(\gamma, t)$ is the unit vector normal to $\Gamma(t)$ at point γ on the contour.

Practically, we represent Γ using a set of nodes that need not be uniformly spaced, but that are resampled if the spacing becomes strongly uneven. Diffusive terms are calculated using a central difference approximation. The area of the cell is given by:

$$A = \frac{1}{2}\sum_{i=1}^{N}(x_i y_{i+1} - x_{i+1}y_i) \tag{19}$$

where (x_i, y_i) are the coordinates of sample point i, and $x_{N+1} \equiv x_1$, $y_{N+1} \equiv y_1$.

In order that the contour resist bending, each sample point acts as the centre of a torsional spring with spring constant k_θ, with the force generated dependent on the difference in the angles to each of its neighbours. The simulation parameters for "wild type" cells are given in Table 1. The simulation parameters for "mutant" cells differed only in two parameters governing membrane tension and stiffness, with $k_\Gamma = 6.0 \times 10^{-6}$ and $k_\theta = 800.0$.

Potential analogues of biochemical species in real cells. Flimamentous actin (F-actin) is crucial for the protrusion of the membrane. It is also self-promoting: polymerised actin interacts with the ARP2/3 complex, initiating the branching (and hence growth) of actin filaments. Given these properties, this species may be a candidate for the local activator. PI3-K may also be a candidate, as it is recruited to the leading edge of cells and

stimulates the conversion of PIP2 to PIP3. Coronin could play the role of the local inhibitor. It is known to inhibit actin filament nucleation, and is observed to co-localise with F-actin *in vivo*. cGMP may act as a global inhibitor. It diffuses quickly and so its conentration would quickly equilibriate across the cell. Mutants unable to synthesise cGMP have been shown to produce excesss, abberant pseudopods (42). Depletion of G-actin may also provide an effective global inhibition mechanism, through long-range competition between pseudopods.

Relation to other models. The Meinhardt model describes a mechanism for autonomous pseudopod formation and modulation by external chemical gradients (21). Like the popular local-excitation, global inhibition (LEGI) model (43), it introduces the concept of a self-promoting activator and a global, inhibitory mechanism that suppresses this activator. This inhibitor ensures that cells only react to signals that are strong relative to the background stimulus they experience, and hence can polarise in favour of a gradient over a range of SNRs. The advantage of the Meinhardt model over the LEGI model is the local inhibitor, which destabilises large, dominant areas of activation. This is crucial as it provides a mechanism for cell reorientation in changing gradients. The LEGI model lacks this element and describes chemosensing only, rather than dealing with motion as a part of chemotaxis. Another advantage of the Meinhardt model is its generality: in using it, we do not make presumptions about the still ill-defined pathways governing eukaryotic chemotaxis. A key drawback of the Meinhardt model is that it does not account for redundant mechanisms, certainly a feature of eukaryotic chemotaxis. Deletion mutants for genes strongly implicated in chemotaxis can often still chemotax, albeit with reduced velocity or efficiency (25).

Our implementation of the Meinhardt model differs from others in its manner of sensing. It is, to our knowledge, the only example which chemosenses as a perfect absorber, *i.e.* using diffusive flux across the boundary. This sensing mechanism is of particular interest as it represents the fundamental physical limit on the accuracy of chemosensing.

References

[34] Canny, J. A Computational Approach to Edge Detection. In *Readings in computer vision: issues, problems, principles, and paradigms*, 184–203 (Morgan Kaufmann, 1987).

[35] Bird, J. L., Eppler, D. T. & Checkley Jr., D. M. Comparisons of herring otoliths using Fourier series shape analysis. *Can. J. Fish. Aquat. Sci.* **43**, 1228–1234 (1986).

[36] Diaz, G., Zuccarelli, A., Pelligra, I. & Ghiani, A. Elliptic Fourier analysis of cell and nuclear shapes. *Comput. Biomed. Res.* **22**, 405 – 414 (1989).

[37] Mebatsion, H., Paliwal, J. & Jayas, D. Evaluation of variations in the shape of grain types using principal components analysis of the elliptic Fourier descriptors. *Comput. Electron. Agr.* **80**, 63 – 70 (2012).

[38] Cootes, T., Taylor, C., Cooper, D. & Graham, J. Active shape models-their training and application. *CVIU* **61**, 38 – 59 (1995).

[39] Christensen, G., Rabbitt, R. & Miller, M. Deformable templates using large deformation kinematics. *IEEE T. Image Process.* **5**, 1435–1447 (1996).

[40] Beg, M. F., Miller, M. I., Trouve, A. & Younes, L. Computing Large Deformation Metric Mappings via Geodesic Flows of Diffeomorphisms. *Int. J. Comp. Vis.* **61**, 139–157 (2005).

[41] Miller, M. I., Trouve, A. & Younes, L. Geodesic Shooting for Computational Anatomy. *J. Math. Imaging Vis.* **24**, 209–228 (2006).

[42] Veltman, D. M. & Van Haastert, P. J. Guanylyl cyclase protein and cgmp product independently control front and back of chemotaxing dictyostelium cells. *Mol. Biol. Cell* **17**, 3921–3929 (2006).

[43] Jin, T., Zhang, N., Long, Y., Parent, C. A. & Devreotes, P. N. Localization of the g protein complex in living cells during chemotaxis. *Science* **287**, 1034–1036 (2000).